Hot-Electron Generation from Laser/Pre-Plasma Interactions in Cone-Guided Fast Ignition

Introduction

The cone-guided scheme for fast-ignition inertial confinement fusion (ICF)[1,2] provides the potential of higher gains at lower total driver energy than conventional central hot-spot–ignition schemes. In this scheme, a spherical target with a hollow gold cone attached is first compressed by laser beams outside the cone and then ignited by a petawatt (PW) short ignition pulse launched into the cone. The cone keeps the plasma out during the compression so that the ignition pulse can reach the cone tip and generate MeV electrons close to the assembled fuel core. Given the angular spread of laser-generated hot electrons, keeping the hot-electron source closer to the assembled core is important to the success of fast ignition. Early Gekko XII experiments with the cone-guided scheme showed good laser–core coupling.[2,3] Recent scaled-up integrated experiments on OMEGA/OMEGA EP showed, however, a lower coupling efficiency.[4]

One of the important factors affecting the laser–core coupling efficiency is the pre-plasma inside the cone.[5] The pre-plasma is generated by an ~1-mJ laser prepulse from amplified spontaneous emission in the PW ignition pulse. Previous experiments and simulations[5–7] have shown that the pre-plasma can significantly reduce the forward-going hot-electron flux. The interaction of the main ignition pulse with the pre-plasma depends on the duration of the ignition pulse, as indicated by recent particle-in-cell (PIC) simulations of laser channeling[8,9] for the channeling/hole-boring fast-ignition scheme. The duration of the short pulse in the early work was of the order of 1 ps (Refs. 5 and 7), and was shorter than the 10-ps pulse in the OMEGA experiment.[4] The required pulse duration for ignition, producing an electron beam with tens of kilojoules of energy,[10] would be 10 to 20 ps. PIC simulations with longer ignition-pulse durations can help answer questions such as whether a longer ignition pulse can essentially push away the pre-plasma to interact mostly with the cone tip.

Here we present recent PIC simulations using *OSIRIS*[11] to study hot-electron generation and their transport in plasma at densities up to 100 n_c, where $n_c = 1 \times 10^{21}$ cm^{-3} is the critical density of 1.053-μm laser light, as used in the cone-in-shell

integrated fast-ignition experiments at the Omega Laser Facility.[4] The simulations are 2-D in space and 3-D in velocity. The pulse duration in the simulations was 6.7 ps, comparable to the 10-ps OMEGA EP pulse. To achieve these simulations, we used an artificial drag force[12] to slow down hot electrons after they leave the laser-interaction region. This prevented the hot electrons from accumulating near the simulation box boundaries and interrupting the simulations. Combined with particle thermal boundary conditions, this also reduced the effects of a finite box size on laser–plasma interactions. The simulations showed that the generated hot electrons were dominated in number by low-energy electrons but in energy by multi-MeV electrons. The hot electrons had a mean half-angle of 68°. Except for differences during the early stage of the pulse, *s*- and *p*-polarizations showed similar accumulated laser-absorption rates and hot-electron characteristics. The electron transport in the density region from 5 n_c to 100 n_c was ballistic, which may make it possible to use the current results for further transport study.

The following sections describe the simulation setup and results, which are then discussed and summarized.

Simulation Setup

The simulation setup is shown in Fig. 134.45(a). Three species of particles were used in the simulations: the electrons (Species 1) and ions (Species 2) initially inside the cone and the electrons initially outside the cone (Species 3). The "cone boundary" in this article refers to the $n_e = 100\,n_c$ surface. The cone boundary had a full opening angle of 34°. The ions outside the cone were treated as immobile. The plasma density profile inside the cone was obtained from linear interpolation of a hydrodynamics simulation using *HYDRA*,[13] in which the laser prepulse had an energy of ~22 mJ and a duration of 0.9 ns. The initial density scale length at n_c was ~20 μm. Densities above 100 n_c (outside the cone) were capped at 100 n_c; therefore, particle transport in plasmas above 100 n_c was not studied. The temperatures of all electrons and gold ions were set at 1 keV. The ionization state of the ions was fixed at 20, estimated based on the *HYDRA* simulation.
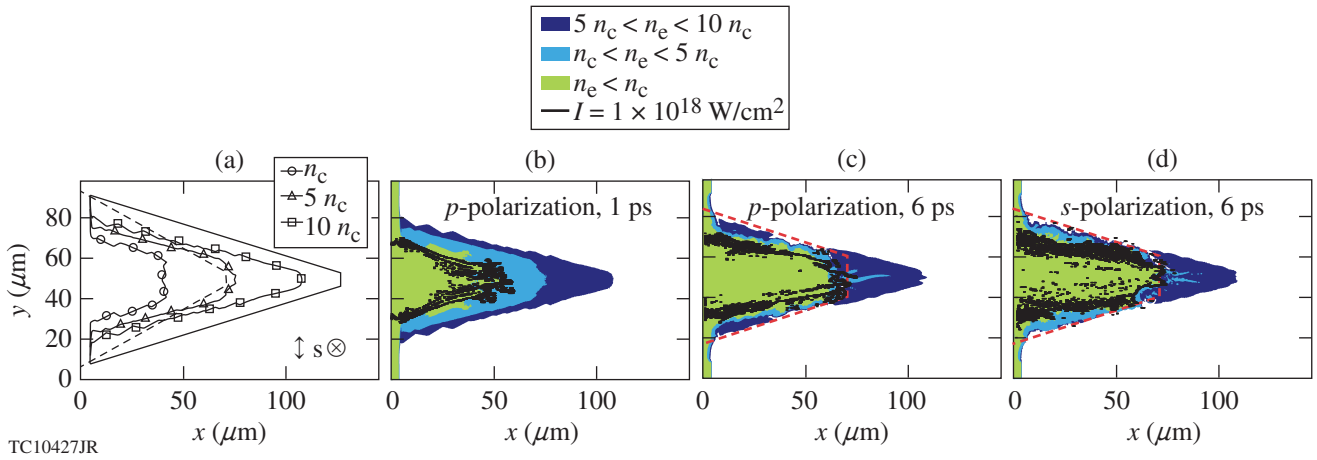
Figure 134.45

(a) Initial setup of pre-plasma inside the cone. The double arrow and the circle with a cross show the oscillation directions of the electric field for p- and s-polarizations. The solid line is the boundary ($100\,n_c$) and the dashed line is the first diagnostic boundary. Plasma density and magnitude of the laser Poynting vector for p-polarization at (b) 1 ps and (c) 6 ps and (d) for s-polarization at 6 ps. The white regions indicate electron density $n_e > 10\,n_c$. The solid black lines show the laser intensity contours of 1.0×10^{18} W/cm^2. In (c) and (d), the red dashed lines are the boundaries for checking charge balance.

The incident laser with wavelength $\lambda = 1.053$ μm was launched at time $t = 0$ from the left side and focused at the cone tip with a peak intensity of 1×10^{19} W/cm^2 and a rise time of 0.56 fs. This short rise time was chosen to speed up the simulation. The transverse profile of the laser intensity was Gaussian with a full width at half maximum (FWHM) of $w_0 = 21$ μm. Both p- and s-polarizations were used in separate simulation runs to infer three-dimensional (3-D) effects. For comparison, the 1.053-μm-wavelength short pulse from OMEGA EP had an energy of ~1 kJ and a 10-ps duration and was focused to a spot with a diameter of $D_{80} = 52 \pm 4$ μm containing 80% of the laser energy. The peak intensity exceeded 1×10^{19} W/cm^2, while the average intensity within D_{80} was several times 10^{18} W/cm^2.

The simulation box size was 150×100 μm. The Cartesian grid sizes dx and dy were set at $0.05\,c/\omega_0 = 7.96 \times 10^{-3}$ μm and the time step at d$t = 0.035/\omega_0 = 1.86 \times 10^{-2}$ fs, where ω_0 and c are the laser-pulse frequency and the speed of light, respectively. The total number of grid cells was $17,856 \times 11,900$. The number of particles per cell was chosen to be 10, 1, and 4 for Species 1, 2, and 3, respectively. For electromagnetic fields, we used open boundary conditions in the x (longitudinal) direction and periodic boundary conditions in the y (transverse) direction.

For particles, a thermal boundary condition was used at all four boundaries; electrons reaching the boundaries were reflected with a new Maxwellian velocity distribution at the initial temperature (1 keV). To prevent hot electrons from accumulating near the boundaries, an artificial drag[12] was introduced on electrons above 30 keV outside the cone

$$\frac{d\vec{v}}{dt} = -\alpha\vec{v}, \tag{1}$$

where $\vec{v}$ is the electron velocity normalized to c and t is the time normalized to $1/\omega_0$. The drag coefficient α was chosen to be 0.0043, which would stop a 1-MeV electron in 17 μm.

The initial density change was represented by a change in the charge weights of the particles while the number of particles per cell was initially constant throughout the simulation box. Therefore, the particles in higher-density regions had larger charge weights than the particles in lower-density regions.

Figure 134.45(a) shows the initial setup for the PIC simulations with different contours matching the critical (n_c), 5-n_c, and 10-n_c density lines inside the cone that were obtained from the *HYDRA* simulation. It is noted that the full-scale plasma in the cone tip was implemented in the simulation and that the target was the same as in the integrated experiments (34° full inner cone angle, 10-μm flat tip, Au cone wall, and pre-plasma). Hot-electron diagnostics were set up at two places as shown in Fig. 134.45(a). The first diagnostic boundary (dashed line) was near the initial $n_e = 5$-n_c surface and the other was at the cone boundary, where $n_e = 100\,n_c$. Whenever an electron passed one of these diagnostic boundaries, its position, momentum, and charge weight were recorded. The incoming and outgoing electrons were separately recorded at these two boundaries. In this article, when calculating hot-electron–related quantities such as average energy, a net distribution function of the hot electrons (>30 keV) was usually used:

TC10427JR

$$f_{\text{hot}} = f_{\text{outgoing}} - f_{\text{incoming}}, \qquad (2)$$

where the flux was normal to the cone boundary. This definition excluded the hot electrons trapped near the boundaries.

Simulation Results

1. Laser Propagation Inside the Cone

To illustrate the laser and plasma evolution inside the cone, we plot the contours of plasma density and the magnitude envelope of the laser Poynting vector at time $t = 1$ ps [Fig. 134.45(b)] and at 6 ps [Fig. 134.45(c)] for the p-polarization case, and at $t = 6$ ps [Fig. 134.45(d)] for the s-polarization case. The initial position of n_c was ~85 μm away from the cone tip and was pushed ~25 μm forward with s-polarization (~60 μm from cone tip) and ~30 μm with p-polarization (~55 μm from cone tip) at 6 ps. At 1 ps, the laser intensity contour of 1.0×10^{18} W/cm^2 interacted with $n_c < n < 5$-n_c plasma. At 6 ps, however, the plasma was pushed transversely to both sides so that the side n_c surface was far from the laser intensity contour of 1.0×10^{18} W/cm^2. In this case hot electrons can be generated only in the underdense plasma. At the end of the simulation ($t = 6.7$ ps), the laser had not reached the original 10-n_c surface, demonstrating the importance of the pre-plasma effect for hot-electron generation inside the cone.

2. Establishment of Return Currents

For the laser to continuously generate hot electrons from the pre-plasma inside the cone during the time considered, there must be a return current drawn from outside the laser–plasma interaction region. Any inhibition of this return current would lead to the buildup of an electrostatic field, preventing further electron acceleration. This could occur numerically as a result of the high weight of the particles in the 100-n_c region, preventing them from moving freely into a region with a density near n_c.

Therefore, the total charges of Species 1 and 3 inside a region defined by the red dashed line in Figs. 134.45(c) and 134.45(d) are plotted as a function of time in Fig. 134.46(a) for p-polarization and Fig. 134.46(b) for s-polarization. The total charge of Species 1 (the electrons originally inside the cone) decreased over time as a result of laser acceleration. In the meantime, Species 3 (the electrons originally outside the cone) moved into the cone to form the return currents, as shown in Figs. 134.46(a) and 134.46(b). The total charge of Species 1 and 3 inside this region was very close to the total charge of Species 2 (the ions, not shown) throughout the simulation, which decreased at later times as the ions were expelled. Similar results were obtained for other regions where $n_e < 3$ n_c and $n_e < 30 \, n_c$. Therefore, the charge was mostly balanced
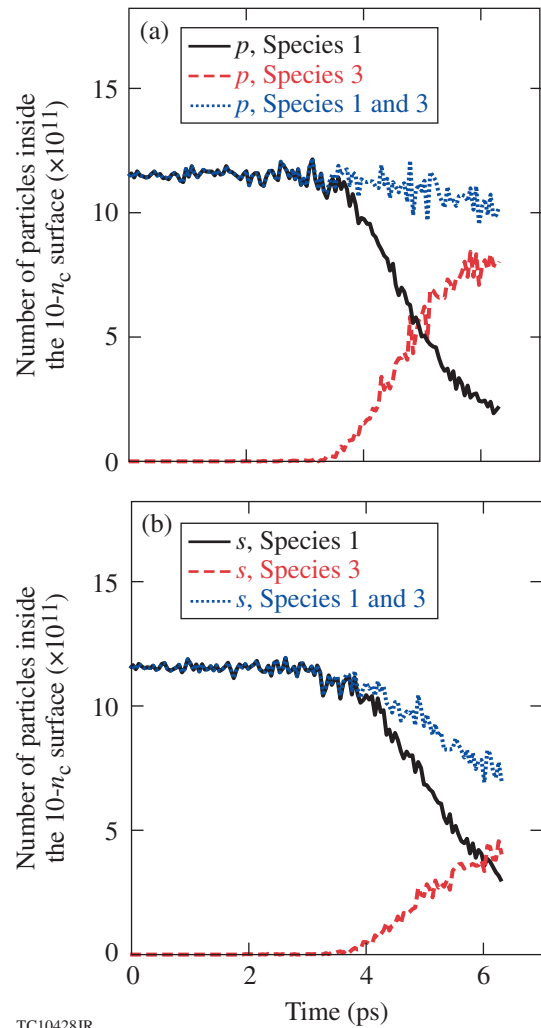

Figure 134.46
Total charge of the electron Species 1 and 3 inside the 10-n_c surface in the unit of electron charge for (a) p-polarization and (b) s-polarization.

and the return current was well established in our simulations. We note that more electrons were pushed out of the cone early for the p-polarized laser beam than for the s-polarized laser beam. We will discuss the reason for this feature in **Energy Density of Electrons** (p. 132).

3. Laser-to-Hot-Electron Conversion Rates and Hot-Electron Energy Spectra

To study how much laser energy was transferred into hot electrons, we define an instantaneous laser-to-hot-electron conversion rate as the total energy of the net outgoing hot electrons normalized by the incident laser energy in a short period of ~0.05 ps. To calculate this rate, the contribution from the incoming hot electrons was subtracted, using Eq. (2). The instantaneous conversion rates of both p- and s-polarized laser

beams are shown in Fig. 134.47(a). Initially, the *p*-polarized laser beam had a higher conversion rate than the *s*-polarized laser beam, but the difference decreased at later times. The conversion rates from 3.5 to 6.7 ps for both cases were about 50%.

The mean energy of the hot electrons is shown in Fig. 134.47(b) as a function of time. The mean energies for the *p*- and *s*-polarized cases reached maximum values of 2 MeV and 1.5 MeV at 0.74 ps and 0.93 ps, respectively; they then decreased over time. This trend was the opposite from that in Ref. 14, where no significant pre-plasma was present, indicating a different hot-electron–generation mechanism in these simulations [see **Energy Density of Electrons** (p. 132)]. After 4 ps, the *p*- and *s*-polarized cases had about the same mean energies.

The energy spectra for accumulated hot electrons for both polarizations are plotted in Fig. 134.47(c). The overall spectra are similar. They can be fitted by a two-temperature function

$$f(E) = 1.06 \times 10^{11} \exp(-E/0.12)$$
$$+ 5.8 \times 10^{8} \exp(-E/3.3), \qquad (3)$$

where E is the electron energy in MeV. The temperature was 0.12±0.03 MeV for the "cold" component (below 500 keV) and 3.3±0.2 MeV for the "hot" component (above 1 MeV). The hot-component temperature was 3.5× the ponderomotive energy (corresponding to the laser intensity of 1×10^{19} W/cm^2) of 0.95 MeV. This again indicates a different hot-electron–generation mechanism from that in previous simulations with no significant pre-plasma.[15]

To describe the spectra in more detail, we define an electron energy fraction function $g(E)$ that is the fraction of the electron energy below E:

$$g(E) = \frac{\int_{30 \text{ keV}}^{E} f(E')E'\,dE'}{\int_{30 \text{ keV}}^{E_{\max}} f(E')E'\,dE'}, \qquad (4)$$

where $f(E)$ is the distribution function of the hot electrons from Eq. (2) and $E_{\max}$ is chosen to be 30 MeV, above which there were few electrons.

Figure 134.47(d) plots $g(E)$ for the accumulated hot-electron spectra for both polarizations. While the mean hot-electron energies at the end of the simulations dropped below 0.5 MeV, the sub-1-MeV electrons contributed only 22% of the total hot-electron energy, as indicated by point A. The electron distribution was dominated by the low-energy electrons in number but by the high-energy electrons in energy. The median energy E_M, defined as $g(E_M) = 0.5$, was much higher than the mean energy of the distribution in Fig. 134.47(b). In Fig. 134.47(d), the median energy E_M was 4.2 MeV for the *p*-polarized case and 3.7 MeV for the *s*-polarized case. These data clearly show that the hot-electron energy is mainly carried by high-energy electrons.

4. Angular Distribution of Hot Electrons
The divergence of the electrons above 1 MeV is one of the quantities critical to the ultimate energy-coupling efficiency in fast ignition. Here, we define the half spread angle of an electron as
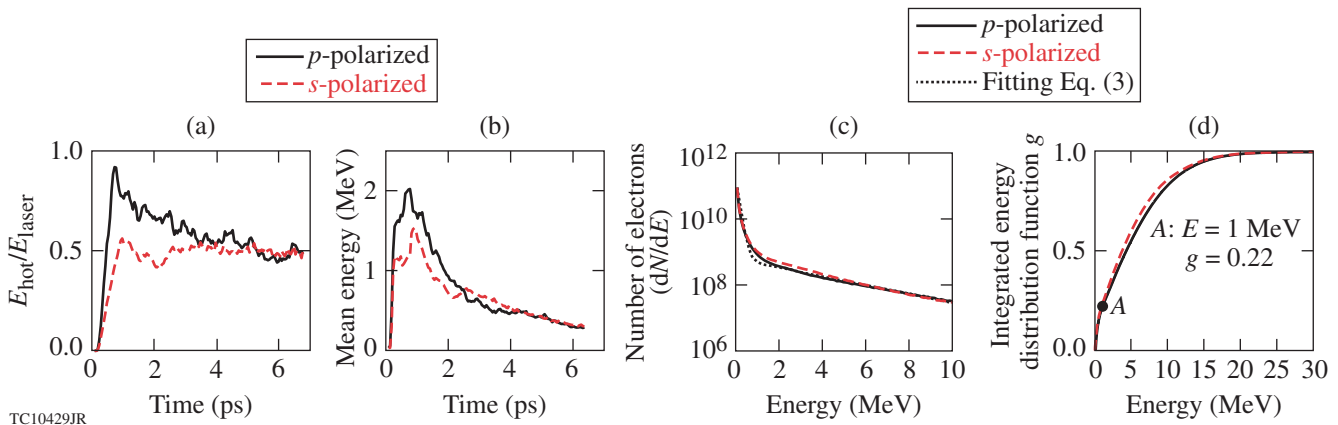

Figure 134.47
(a) Instantaneous laser-to-hot-electron conversion rate; (b) mean energy of the outgoing hot electrons; (c) accumulated hot-electron energy spectra and the fitting [Eq. (3)]; and (d) function *g* in Eq. (4) for accumulated hot electrons. All plots are shown for both *p*- and *s*-polarization cases.

$$\theta = \tan^{-1}\left(\frac{p_y}{p_x}\right), \qquad (5)$$

where p_x and p_y are the momenta of the electron in the x and y directions.

Since the hot electrons were dominated in number by low-energy electrons, we plot the normalized angular distribution of hot electrons with and without energy weighting in Fig. 134.48(a). These distributions show that a significant amount of energy was carried by electrons with a large θ. The energy-weighted, mean half-angle

$$\sum_i \theta_i q_i E_i \bigg/ \sum_i q_i E_i$$

of the hot electrons is plotted in Fig. 134.48(b), where q_i and E_i are the charge weight and kinetic energy of each particle, respectively. The mean half-angle for the accumulated distribution increased slightly over time and was between 58° and 68°.

5. Ballistic Electron Motion Inside the Cone

A realistic electron source is vital for the transport study of hot electrons in fast ignition.[10,15–17] Figure 134.49 plots the energy-weighted angular spread and energy spectra from
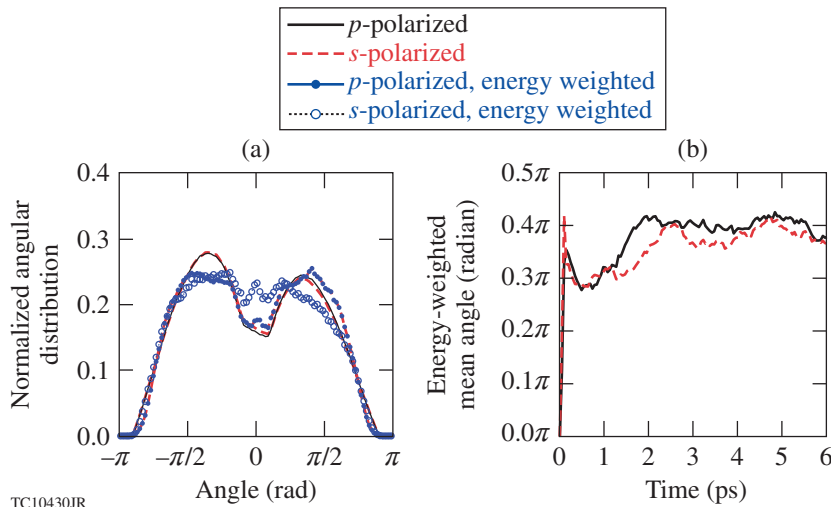

Figure 134.48
(a) Normalized angular distribution of accumulated hot electrons with and without energy weighting; (b) energy-weighted mean angle of accumulated hot electrons versus time for p- (solid) and s-polarization (dashed).
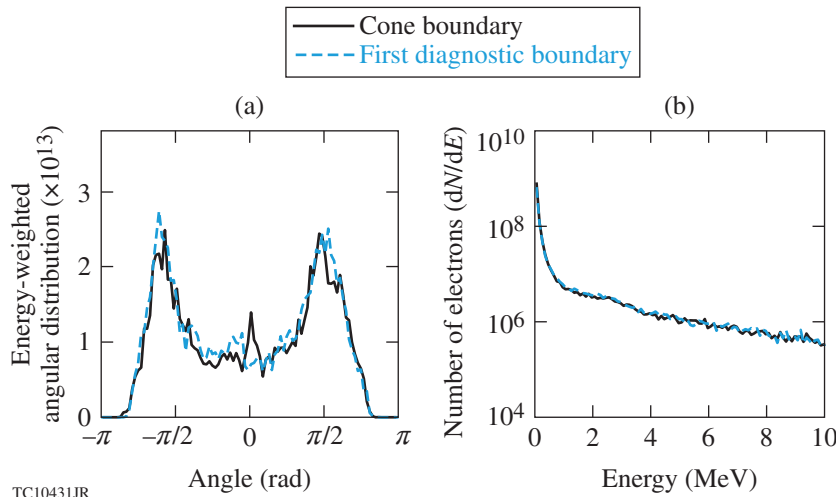

Figure 134.49
(a) Energy-weighted angular distribution at 1.96 ps < t < 2.01 ps and (b) corresponding energy spectrum recorded at the cone boundary (solid) and the first virtual boundary (dashed).

both the first diagnostic boundary [see Fig. 134.45(a)] and the cone boundary at 1.96 ps < t < 2.01 ps. The similarity of the electron characteristics shows that the transport between the two boundaries was mostly ballistic. This makes it possible to build an electron source from the information collected at the cone boundary for future transport study.

6. Energy Density of Electrons

The observed hot-electron characteristics, including the accumulated energy and angular distributions and the long-term laser-to-hot-electron conversion rates, were similar for p- and s-polarizations. Significant differences existed only early in time (Fig. 134.47), indicating that some of the known laser-heating mechanisms operating only in p-polarization, such as resonant[18,19] and Brunel[20] heating, were not dominant in these simulations. To further illustrate this, the electron energy densities at two different times for both polarizations are plotted in Fig. 134.50. The normalized electron energy density is defined as

$$h(x,y) = n_e(x,y)\bar{E}_k(x,y)/(n_c mc^2),\qquad(6)$$

where $n_e(x,y)$ is the total electron density, including both Species 1 and 3; $\bar{E}_k(x,y)$ is the mean kinetic energy of local electrons; and n_c, m, and c are the previously defined quantities. Initially, with the uniform electron temperature $T_e = 1$ keV, $h(x,y)$ was in the range [0, 0.3]. When hot electrons are present, $h(x,y)$ can increase to the range [1, 3], as shown by the regions in black in Fig. 134.50. Therefore, Fig. 134.50 essentially plots the hot-electron energy density.

At 1 ps [Figs. 134.50(a) and 134.50(b)], both polarizations show the highest hot-electron densities in the laser region and hot-electron fluxes in the forward direction. For p-polarization, however, additional fluxes were propagating sideways. The sideways fluxes had a modulated structure with a wavelength close to the laser wavelength λ. They appeared to originate from the edge of the laser beam, where the electron density was approximately n_c and the density scale length was $\sim\lambda$ [see also Fig. 134.45(b)]. This indicates that Brunel heating[20] was the likely generation mechanism for these sideways hot electrons and accounts for the higher conversion rate for the p-polarization in Fig. 134.47(a). The return current for the p-polarization also emerged earlier in Fig. 134.46(a).

At 6 ps, more sideways fluxes appeared for both polarizations [Figs. 134.50(c) and 134.50(d)]; however, these fluxes did not have a modulated structure, indicating that they were no longer generated by the Brunel mechanism. This is also corroborated by the fact that the n_c surface moved away from the laser region [Figs. 134.45(c) and 134.45(d)]. Most hot electrons were likely generated stochastically through interactions of the laser pulse with the underdense plasma. From particle trajectories, we observed many hot electrons passing through the laser region multiple times before crossing the cone boundary. Actual heating processes are difficult to analyze but they can be a high-intensity analog of the stochastic heating from mode coupling in parametric instabilities[21] and/or the stochastic heating from the laser pulse and its reflection.[22,23] The electrons can be heated stochastically to an energy much higher than the laser ponderomotive potential.[24] The sideways fluxes in
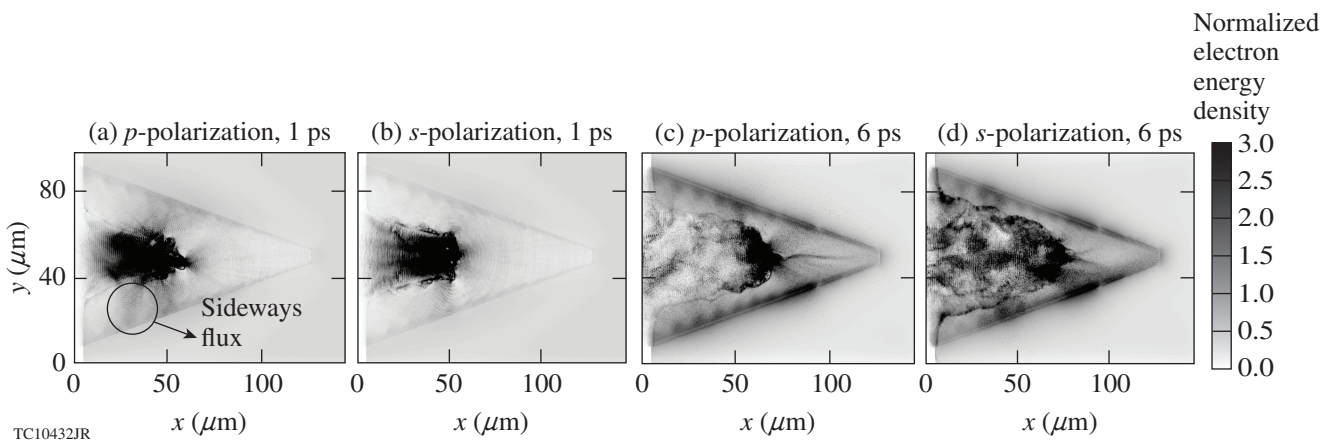

Figure 134.50
Energy density of all electrons (Species 1 and 3) for a p-polarized laser beam at (a) 1 ps and (c) 6 ps and for an s-polarized laser beam at (b) 1 ps and (d) 6 ps.

Figs. 134.50(a) and 134.50(b) explain the large spreading angles in Figs. 134.48(a) and 134.48(b). The stochastic heating is independent of the polarization direction and the hot electrons generated are relatively isotropic. The large spreading angles observed here have a different origin from the deformation of the laser/overdense-plasma interface observed in previous simulations where no significant pre-plasmas were present.[14,25,26]

Discussion and Summary

Figure 134.51 compares several measured electron spectra from the integrated experiments[4] and the simulated spectrum of the outgoing electrons. In the experiment, fast electrons that escaped the target were recorded in two different directions: in the laser's forward direction [Fig. 134.51(a)] and sideways [Fig. 134.51(b)] at an angle of 79° to the laser-beam axis. For the

simulation, the simulated outgoing electrons with an absolute angle of less than 9° and between 70° and 88°, respectively, were considered as forward and sideways electrons. They are also plotted in Fig. 134.51 multiplied by a factor of 20 to allow for a better comparison with the experimental data. The choice of an angular range of $\pm 9°$ is arbitrary but justified by the fact that over this range, the shape of the simulated electron spectrum was uniform. Despite the shot-to-shot fluctuations in the measured spectra, the experimental and simulated spectra are remarkably similar in the high-energy region above ~10 MeV. A quantitative comparison of the simulated and measured spectra over the entire energy range is made difficult by the fact that the escaped electrons measured in the experiments were influenced by the electron transport in the dense ($n_e > 100\ n_c$) plasmas, which was not simulated here. Strong self-generated electric and magnetic fields in the dense plasma region would affect the directionality of lower-energy electrons (≤ 1 MeV) and were not taken into account in the simulation data. It is expected, however, that the high-energy tail of the escaped electrons was less influenced by the transport and that inferred slope temperatures should be comparable. Figure 134.52 shows the inferred slope temperatures from the electron spectra in the 10- to 20-MeV energy range of Fig. 134.51. The circles correspond to the spectra in the forward direction and the triangles correspond to the sideways spectra. The square
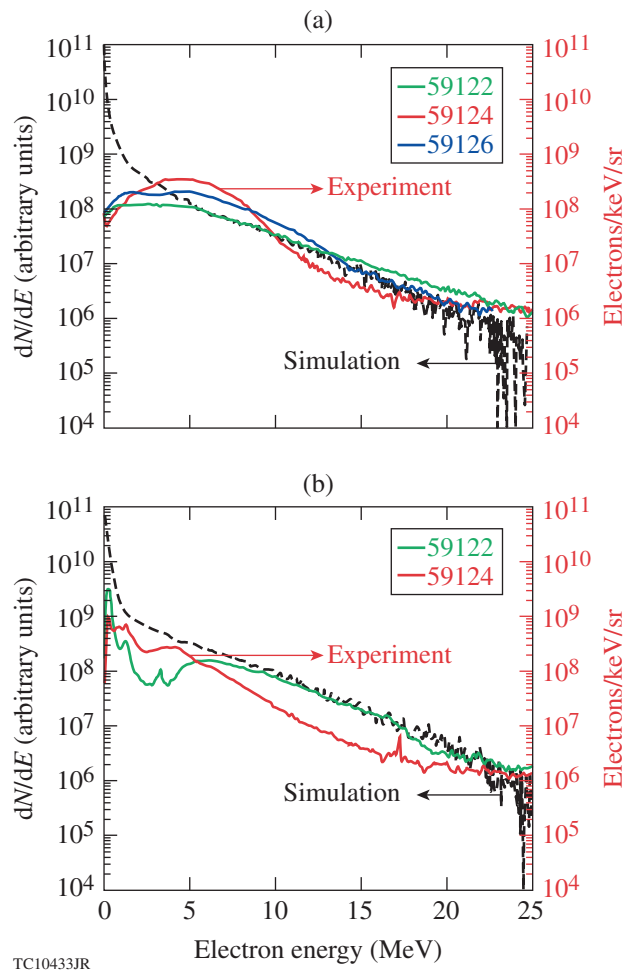

Figure 134.51
Comparison of measured (solid) and simulated (dashed) electron spectra in (a) the laser's forward direction and (b) approximately 79° to the laser-beam direction.[4]
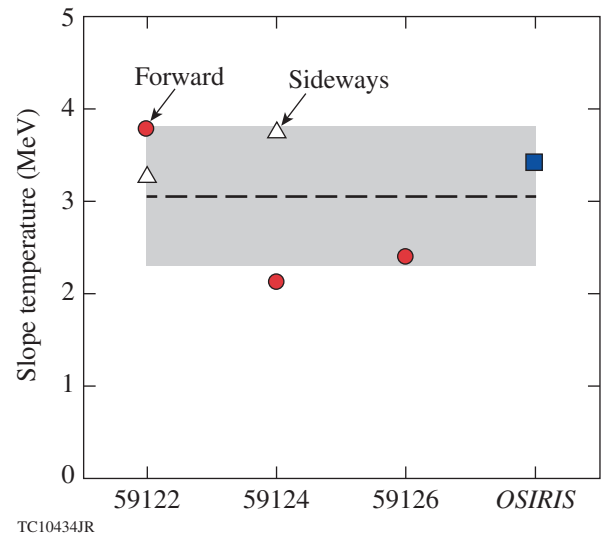

Figure 134.52
Inferred slope temperature from the electron spectra in Fig. 134.51 in the 10- to 20-MeV energy range. The circles correspond to the spectra in the forward direction and the triangles correspond to the sideways spectra. The square represents the simulation result. The dashed line is the average of the five measurements and the gray band represents the measurement uncertainty (range equal to twice the standard deviation).

represents the simulated temperature. The dashed line is the average of the five measurements, 3.05 MeV, which is close to the simulated value of 3.4 MeV within the measurement uncertainty (gray band). This shows good agreement between the simulation and the experiment. The laser–core energy coupling rate in the simulation is estimated by assuming the compressed dense deuterated plastic core is 115 μm away from the laser–plasma interface with an areal density of 0.1 g/cm^2 and a diameter of 160 μm. These conditions were obtained from the previous hydrodynamic simulations of the implosion.[27] With the assumption of ballistic motion, hot electrons with a deflection angle smaller than 35° can reach the dense core and deposit energy there. Considering the different energy-deposition rates of hot electrons with different energies, the total energy-coupling rate from laser beam to the dense core is ~0.9%, which is less than the 3.5±1.0% estimation from the integrated-experiment results. There are two possible reasons for the inconsistency. First, a self-generated magnetic field could exist that can couple the electrons with a larger deflection angle to the core.[9,28] Second, the neutrons might be generated by fast-electron–induced shocks in the core plasma. Such shocks can be generated either by direct heating of the core by fast electrons or by hydrodynamic expansion of the gold cone heated by fast electrons to ~1 keV (Ref. 4). A significant number of electrons were recorded in the sideways direction, corroborating a large divergence angle of the electrons. The large hot-electron spread angles found here can qualitatively explain the low laser–core coupling in these experiments. It is worth noting that recent integrated-experiments[29] using Cu-doped shells and monochromatic imaging of the Cu K_α fluorescence emission induced by the fast electrons also showed that a significant amount of hot electrons hit the side wall of the cone, which is again an indication of the large angular spread of the electrons consistent with the simulations. These simulations will help us gain a further understanding of the integrated experiments, and the hot-electron source from the simulations can be used in transport studies.

In summary, we have studied the properties of hot electrons generated during laser/pre-plasma interactions in cone-guided fast ignition over 6.7 ps using PIC simulations. Hot electrons were generated mainly through stochastic heating, which produced similar hot-electron characteristics for *p*- and *s*-polarizations in 2-D, indicating that this will also be the case in 3-D. The laser-to-hot-electron conversion rate approached 50%. Electrons with energy <300 keV dominated in number in the distribution but 78% of the hot-electron energy was carried by electrons with energy above 1 MeV. The hot electrons

had an energy-weighted mean half-angle of 68°. The electron transport in the 5-n_c to 100-n_c region was ballistic. These results provide further evidence of the detrimental effects of pre-plasma in the cone.

ACKNOWLEDGMENT

REFERENCES

1. M. Tabak *et al.*, Phys. Plasmas **1**, 1626 (1994).

2. R. Kodama *et al.*, Nature **412**, 798 (2001).

3. R. Kodama *et al.*, Nature **418**, 933 (2002).

4. W. Theobald, A. A. Solodov, C. Stoeckl, K. S. Anderson, R. Betti, T. R. Boehly, R. S. Craxton, J. A. Delettrez, C. Dorrer, J. A. Frenje, V. Yu. Glebov, H. Habara, K. A. Tanaka, J. P. Knauer, R. Lauck, F. J. Marshall, K. L. Marshall, D. D. Meyerhofer, P. M. Nilson, P. K. Patel, H. Chen, T. C. Sangster, W. Seka, N. Sinenian, T. Ma, F. N. Beg, E. Giraldez, and R. B. Stephens, Phys. Plasmas **18**, 056305 (2011).

5. A. G. MacPhee *et al.*, Phys. Rev. Lett. **104**, 055002 (2010).

6. H. Shiraga *et al.*, Plasma Phys. Control. Fusion **53**, 124029 (2011).

7. S. D. Baton *et al.*, Phys. Plasmas **15**, 042706 (2008).

8. G. Li *et al.*, Phys. Rev. Lett. **100**, 125002 (2008).

9. G. Li *et al.*, Phys. Plasmas **18**, 042703 (2011).

10. A. A. Solodov, K. S. Anderson, R. Betti, V. Gotcheva, J. Myatt, J. A. Delettrez, S. Skupsky, W. Theobald, and C. Stoeckl, Phys. Plasmas **15**, 112702 (2008).

11. R. A. Fonseca *et al.*, Lect. Notes Comput. Sci. **2331**, 342 (2002).

12. J. Tonge *et al.*, Phys. Plasmas **16**, 056311 (2009).

13. M. M. Marinak *et al.*, Phys. Plasmas **3**, 2070 (1996).

14. A. J. Kemp and L. Divol, Phys. Rev. Lett. **109**, 195005 (2012).

15. D. J. Strozzi *et al.*, Phys. Plasmas **19**, 072711 (2012).

16. J. J. Honrubia and J. Meyer-ter-Vehn, Nucl. Fusion **46**, L25 (2006).

17. T. Johzaki, Y. Nakao, and K. Mima, Phys. Plasmas **16**, 062706 (2009).

18. D. W. Forslund *et al.*, Phys. Rev. A **11**, 679 (1975).

19. K. Estabrook and W. L. Kruer, Phys. Rev. Lett. 40, **42** (1978).

20. F. Brunel, Phys. Rev. Lett. **59**, 52 (1987).

21. J. J. Thomson, R. J. Faehl, and W. L. Kruer, Phys. Rev. Lett. **31**, 918 (1973).

22. Z.-M. Sheng *et al.*, Phys. Rev. Lett. **88**, 055004 (2002).

23. Z.-M. Sheng *et al.*, Phys. Rev. E **69**, 016407 (2004).

24. S. C. Wilks *et al.*, Phys. Rev. Lett. **69**, 1383 (1992).

25. A. Debayle *et al.*, Phys. Rev. E **82**, 036405 (2010).

26. H. Schmitz, R. Lloyd, and R. G. Evans, Plasma Phys. Control. Fusion **54**, 085016 (2012).

27. A. A. Solodov, M. Theobald, A. S. Anderson, A. Shvydky, R. Betti, J. F. Myatt, and C Stoeckl, Bull. Am. Phys. Soc. **57**, 29 (2012).

28. A. A. Solodov, K. S. Anderson, R. Betti, V. Gotcheva, J. F. Myatt, J. A. Delettrez, S. Skupsky, W. Theobald, and C. Stoeckl, Phys. Plasmas **16**, 056309 (2009).

29. L. C. Jarrott, M. S. Wei, A. A. Solodov, H. Sawada, R. B. Stephens, A. Greenwood, D. Hoover, N. Alfonso, H. Huang, E. Giraldez, W. Theobald, C. Stoeckl, F. J. Marshall, J. Delettrez, R. Betti, P. K. Patel, H. McLean, C. Chen, M. K. Key, H. Chen, T. Doeppner, T. Yabuuchi, H. Habara, and F. N. Beg, presented at the 2012 Stewardship Science Academic Alliances (SSAA) Symposium, Washington, D.C., 22 February 2012.